

RESEARCH ARTICLE

10.1002/2017JD026632

Key Points:

- Tropical Tropopause Layer relative humidity distribution over Pacific examined
- Lower TTL is humid over the western Pacific and dry over the central/eastern Pacific
- Convection and vertical motions drive the TTL distribution of relative humidity

Correspondence to:

E. J. Jensen,
eric.jensen@nasa.gov

Citation:

Jensen, E. J., et al. (2017), Physical processes controlling the spatial distributions of relative humidity in the tropical tropopause layer over the Pacific, *J. Geophys. Res. Atmos.*, 122, 6094–6107, doi:10.1002/2017JD026632.

Received 10 FEB 2017

Accepted 29 MAY 2017

Accepted article online 1 JUN 2017

Published online 13 JUN 2017

Physical processes controlling the spatial distributions of relative humidity in the tropical tropopause layer over the Pacific

Eric J. Jensen¹, Troy D. Thornberry^{2,3}, Andrew W. Rollins^{2,3}, Rei Ueyama¹, Leonhard Pfister¹, Theopaul Bui¹, Glenn S. Diskin⁴, Joshua P. DiGangi⁴, Eric Hints^{3,5}, Ru-Shan Gao², Sarah Woods⁶, R. Paul Lawson⁶, and Jasna Pittman^{7,8}

¹Atmospheric Science Branch, NASA Ames Research Center, Moffett Field, California, USA, ²Chemical Sciences Division, NOAA Earth System Research Laboratory, Boulder, Colorado, USA, ³Cooperative Institute for Research in Environmental Sciences, University of Colorado Boulder, Boulder, Colorado, USA, ⁴Chemistry and Dynamics Branch, NASA Langley research Center, Hampton, Virginia, USA, ⁵Global Monitoring Division, NOAA Earth System Research Laboratory, Boulder, Colorado, USA, ⁶SPEC, Inc., Boulder, Colorado, USA, ⁷Northwest Research Associates, Seattle, Washington, USA, ⁸School of Engineering and Applied Sciences, Harvard University, Cambridge, Massachusetts, USA

Abstract The spatial distribution of relative humidity with respect to ice (RHI) in the boreal wintertime tropical tropopause layer (TTL, ≈ 14 – 18 km) over the Pacific is examined with the measurements provided by the NASA Airborne Tropical Tropopause EXperiment. We also compare the measured RHI distributions with results from a transport and microphysical model driven by meteorological analysis fields. Notable features in the distribution of RHI versus temperature and longitude include (1) the common occurrence of RHI values near ice saturation over the western Pacific in the lower to middle TTL; (2) low RHI values in the lower TTL over the central and eastern Pacific; (3) common occurrence of RHI values following a constant mixing ratio in the middle to upper TTL (temperatures between 190 and 200 K); (4) RHI values typically near ice saturation in the coldest airmasses sampled; and (5) RHI values typically near 100% across the TTL temperature range in air parcels with ozone mixing ratios less than 50 ppbv. We suggest that the typically saturated air in the lower TTL over the western Pacific is likely driven by a combination of the frequent occurrence of deep convection and the predominance of rising motion in this region. The nearly constant water vapor mixing ratios in the middle to upper TTL likely result from the combination of slow ascent (resulting in long residence times) and wave-driven temperature variability. The numerical simulations generally reproduce the observed RHI distribution features, and sensitivity tests further emphasize the strong influence of convective input and vertical motions on TTL relative humidity.

1. Introduction

Water vapor in the upper troposphere/lower stratosphere (UTLS) region has a significant impact on the budget of outgoing longwave radiation and climate [Forster and Shine, 2002; Riese et al., 2012], and even small changes in UTLS humidity can modulate tropospheric warming driven by increasing greenhouse gases on decadal time scales [Solomon et al., 2010]. Upper tropospheric humidity is regulated by transport and cirrus cloud processes, and the relative humidity distribution, in turn, determines when and where cirrus form. The physical processes controlling humidity in the tropical tropopause layer (TTL; ≈ 14 – 18 km) are of particular interest because ascent through the TTL is the primary source of air to the stratosphere, and the concentration of H₂O passing through the tropical tropopause cold trap determines (along with methane oxidation) the humidity of the entire stratosphere.

TTL water vapor concentration can also serve as a useful tracer for transport and cloud processes in the region. Outside of deep convective cloud systems, air in the TTL above about 13–15 km generally ascends slowly in balance with radiative heating, whereas radiative cooling and subsidence prevail below this level [Gettelman et al., 2004]. Given the strong dependence of TTL radiative heating rate on cloud distributions, the heating rate profile varies considerably with season and geographic location [Yang et al., 2010]. Since water vapor mixing ratio is conserved in the absence of cloud formation, the relative humidity increases in rising, cooling air and correspondingly decreases in descending air. Rapid vertical ascent of moisture- and ice-laden air in

deep convection provides an important source of water vapor to the TTL, particularly in the lower TTL [Ueyama *et al.*, 2015]. In situ formation of thin cirrus in the upper TTL, primarily driven by transport through cold regions [Holton and Gettelman, 2001] and wave-induced temperature anomalies [Kim *et al.*, 2016], provides a sink for water vapor.

Global satellite measurements of TTL water vapor generally involve broad weighting functions resulting in vertical resolution no better than 2–3 km. The high altitudes of the TTL make it inaccessible to most research aircraft. Past TTL measurements using hygrometers on specialized, high-altitude aircraft and balloon-borne hygrometers have been relatively sparse [Kley *et al.*, 1982; Kelly *et al.*, 1993; Kley *et al.*, 1997; Weinstock *et al.*, 1994; Vömel *et al.*, 2002; Jensen *et al.*, 2008; Schiller *et al.*, 2009; Krämer *et al.*, 2009], and unresolved discrepancies between water vapor concentrations measured with different instruments have generally hindered quantitative analyses of TTL relative humidity statistics [Fahey *et al.*, 2014]. The recent Airborne Tropical Tropopause Experiment (ATTREX) provided extensive, accurate, high vertical resolution measurements of water vapor concentration, temperature, cloud properties, and chemical tracers through the vertical depth of the TTL and spanning the longitudinal extent of the tropical Pacific [Jensen *et al.*, 2016b]. Here we use this data set to investigate the vertical and longitudinal distributions of TTL relative humidity over the Pacific. Using the data in combination with numerical simulations of TTL transport, cloud formation, and humidity, we investigate the physical processes responsible for establishing the observed relative humidity distributions.

The paper is structured as follows: section 2 describes the ATTREX measurements used. Section 3 describes the Pacific TTL meteorological environment, including the climatology of deep convection influencing the air masses sampled. Section 4 discusses the observed TTL relative humidity distributions. Section 5 discusses the results from transport/cloud simulations of TTL relative humidity. A summary and discussion is provided in section 6.

2. ATTREX Measurements of TTL Relative Humidity, Clouds, and Tracers

The ATTREX Global Hawk flights during late winter/early spring of 2013 and 2014 provided extensive sampling of the TTL across the Pacific (Figure 1). The 2013 flights from NASA Armstrong Flight Research Center in California provided sampling over the central and eastern Pacific (centeastPac) and the 2014 flights from Guam sampled the western Pacific (westPac). The primary sampling strategy used for the Global Hawk flights was to profile continuously between about 14 km and the aircraft ceiling (≈ 16 –19 km, depending on the remaining fuel load), with relatively brief level segments at the bottoms and tops of these profiles. Overall, the ATTREX campaigns provided about 300 vertical profiles through the TTL.

Given the critical importance of water vapor measurements for the ATTREX science objectives involving dehydration of air entering the stratosphere, two hygrometers were included in the Global Hawk payload, both of which were sensitive enough to provide good accuracy and precision at the low mixing ratios encountered in the tropical tropopause layer.

The NOAA-H₂O two-channel, internal-path tunable diode laser hygrometer measured both water vapor (using a sideways-facing inlet) and enhanced total water (using a forward facing inlet) [Thornberry *et al.*, 2015]. An onboard calibration system is used to ensure measurement accuracy during flight; the measurement has a 5% fractional uncertainty from the calibration and a 0.23 ppmv absolute uncertainty set by the spectral fringes. [Thornberry *et al.*, 2015]. Condensed-phase water (ice crystals) was enhanced by a factor of about 30–50, depending on altitude and airspeed. Measured ice crystal size distributions during ATTREX indicate that the error in the derived cloud ice water content (IWC) due to particle size dependence of the enhancement factor is less than 2% for 95% of the observations [Rollins *et al.*, 2016]. Overall uncertainty in the IWC determination is estimated to be 20%.

The diode laser hygrometer (DLH) instrument is an external-path tunable diode laser hygrometer that achieves a long path (12.2 m) by directing the laser beam from the fuselage to a reflector on the wing and measuring the return signal. As a result, this instrument achieves high precision (50 ppbv for a 20 Hz data rate) and good accuracy ($\approx 10\%$) even under dry TTL conditions [Podolske *et al.*, 2003]. The agreement between water vapor concentrations measured by NOAA-H₂O and DLH during ATTREX was excellent [Jensen *et al.*, 2016b].

Calculation of accurate relative humidities also requires accurate measurements of temperature. Calibrated temperature, pressure, and wind velocity were measured with the Meteorological Measurement System (MMS)

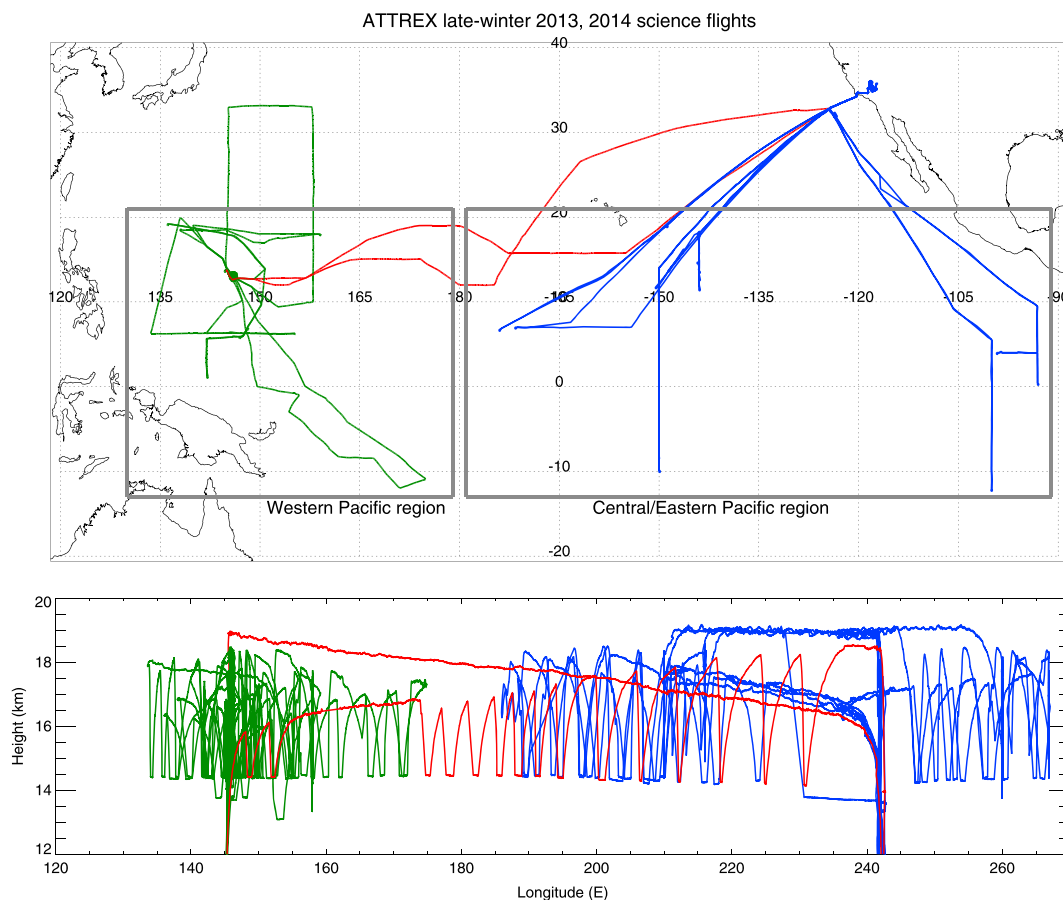


Figure 1. (top) ATTREX flight tracks and (bottom) height profiles. The 2013 flight paths are shown with blue lines, and the 2014 flight paths are green (Guam local flights) and red (transits) lines. The subsets of flights in the westPac and centeastPac regions are indicated by the grey boxes.

on board the Global Hawk. The MMS measurements include corrections for aircraft attitude (pitch, roll, and yaw) changes, and the combined uncertainty in MMS temperature is about 0.3 K [Scott *et al.*, 1990]. The resulting uncertainty in relative humidity is no larger than about $\pm 15\%$.

For distinguishing sampling times inside TTL cirrus from clear-sky segments, we use the Fast Cloud Droplet Probe (FCDP), which measures the scattering from individual ice crystals and infers the particle size [O'Connor *et al.*, 2008; Lance *et al.*, 2010], and the Two-Dimensional Stereo Probe (2D-S) that images individual ice crystals [Lawson *et al.*, 2006]. We define in-cloud measurements as those with both FCDP and 2D-S ice concentrations greater than 15 L^{-1} . Clear-sky regions are defined as those with ice detected by neither FCDP nor 2D-S. Note that during the 2013 flights, the 2D-S data were not available because the Hawkeye probe was not flown. Using a somewhat larger threshold for the clear-sky subset has very little impact on the RHI distributions. This makes sense since very low ice concentration cirrus do not effectively quench ice supersaturation. Using a smaller ice concentration threshold for the in-cloud subset slightly increases the spread of RHI around 100%. This dependence makes physical sense since the supersaturation quenching time increases with decreasing ice concentration.

We also use ozone measurements to subdivide the RHI measurements based on air mass origin. During the 2014 ATTREX westPac campaign, ozone was measured with a Model 205 UV photometer from 2B technologies providing 5 s samples (E. Hints, personal communication). During the 2013 ATTREX campaign, ozone was measured with the NOAA dual-beam UV absorption photometer providing 2 Hz samples [Gao *et al.*, 2012]. The latter instrument provided greater precision, but the accuracy and precision of both instruments are adequate for the current purpose of general subdivision of RHI measurements into low, middle, and high ozone concentration regimes.

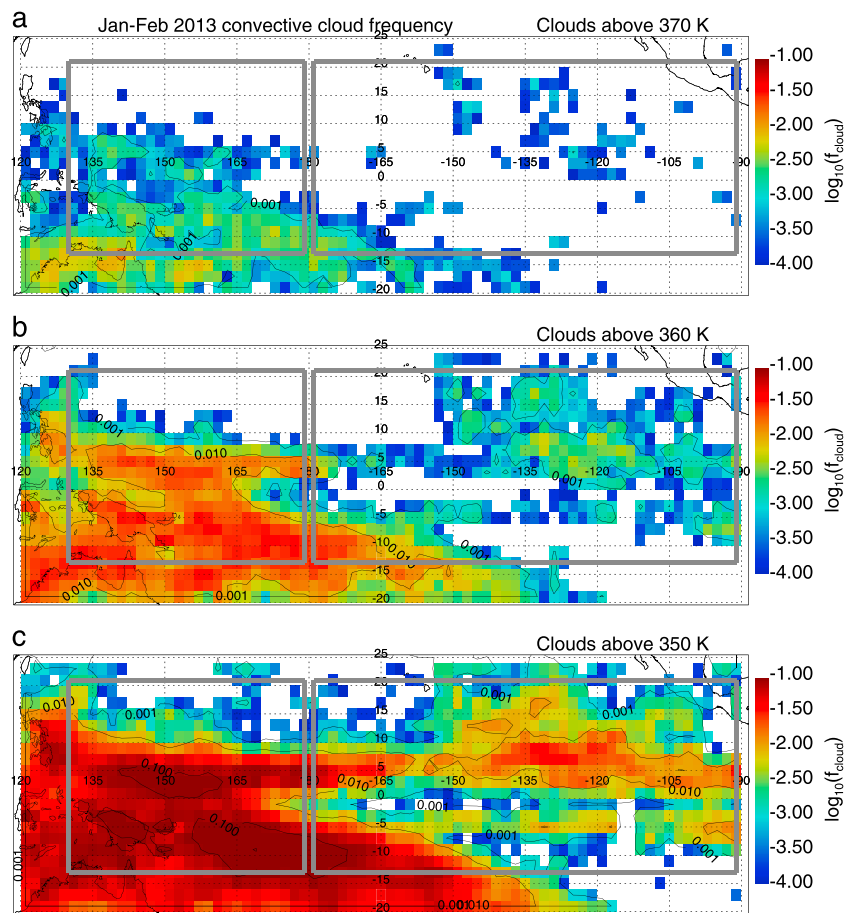


Figure 2. Occurrence frequency of convection extending above potential temperatures of (a) 370, (b) 360, and (c) 350 K during January–February 2013. The cloud top heights are derived from geostationary satellite infrared measurements, with TRMM precipitation measurements used to distinguish convective clouds from in situ cirrus. The grey boxes indicate the westPac and centeastPac regions discussed in the text.

3. Meteorological Setting

As discussed above, rapid vertical transport in deep convection is an important source of water in the TTL. The ice crystals detrained from deep convection tend to sediment out relatively quickly, ultimately leaving behind a volume of ice saturated air (relative humidity with respect to ice near 100%). We derive the frequency distribution of convective clouds extending into the TTL from geostationary satellite measurements of infrared cloud top and precipitation [Pfister *et al.*, 2001; Bergman *et al.*, 2012]. The cloud top heights determined from infrared brightness temperatures are adjusted to provide a statistical match with CALIPSO lidar measurements of cloud tops. Figure 2 shows the convective cloud frequency above different potential temperature levels over the Pacific region for January–February 2013; the January–February 2014 convective cloud distribution is very similar to 2013. Convection extending into the lower TTL (up to about 360 K) is common the westPac region south of about 10°N, with convection occasionally extending into the upper TTL in the southern part of the westPac region. Deep convection reaching the TTL is far less common in the centeastPac region, with occurrence frequencies generally less than 1%.

Following Pfister *et al.* [2001] and Ueyama *et al.* [2014], we determine the time since most recent encounters with deep convection for air masses along the flight tracks by running diabatic back trajectories from the flight track locations and times, and tracing the trajectories through fields of convective cloud top height derived from the 3-hourly geostationary satellite infrared brightness temperature and precipitation fields. We use 40 day trajectories launched along the ATTREX flight tracks. The trajectory launch locations along the flight tracks are chosen to be no more than 0.2° apart; in aircraft ascents and descents, closer spacing is used such that the vertical separation between two consecutive trajectory launch locations is no more than 0.15 km.

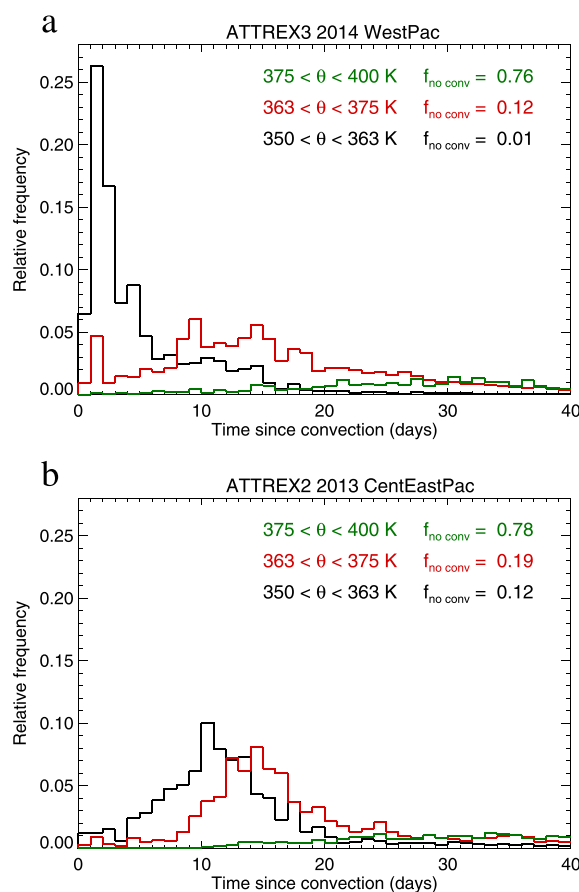


Figure 3. Frequency distributions of days since most recent convective encounter are plotted based on trajectory analysis from times and locations along the ATTREX flight paths. (a) The 2014 western Pacific flights; (b) 2013 central/eastern Pacific flights. Different colors correspond to flight segments in different ranges of potential temperature corresponding to the different temperature regimes in the RHI distributions. The fraction of time along the flight tracks for which back trajectories did not intersect convection within 40 days is indicated in the legend. More recent convective influence in the western Pacific is apparent, particularly in the lower TTL.

ing only the parcels that intersected convection within 40 days in this lower TTL layer, the median time since most recent convection was 3.0 days in the westPac and 12.3 days in the centeastPac. Also, essentially, all air masses sampled in the westPac lower TTL intersected convection within 40 days, whereas 12% of air masses sampled in the centeastPac lower TTL did not encounter convection along the 40 day back trajectories. In the middle (363–375 K potential temperature) and upper (375–400 K potential temperature) TTL, the mean time since convective influence and fraction of air masses that intersected deep convection are comparable in the westPac and centeastPac regions.

The TTL relative humidity along the aircraft flight tracks is also necessarily affected by both the temperatures at the sampling locations as well as the temperature histories of the air masses sampled. Air parcels that experienced cold temperatures prior to the measurement times will have been dehydrated by cloud formation and ice sedimentation. If the air parcels are then advected into much warmer regions, the relative humidity can be quite low. We use the trajectories described above to investigate the temperature histories experienced by air parcels along the flight paths. Figure 4 shows the height distributions of mean temperatures along the aircraft flight tracks as well as the mean minimum temperatures experienced along the 40 day back trajectories versus the potential temperature along the flight track. The most prominent difference between the 2014 (westPac) and 2013 (centeastPac) temperature statistics is the much warmer final temperatures along

ERA-Interim wind and temperature fields are used. Vertical motion is diagnosed using the off-line calculations of radiative heating by Yang *et al.* [2010]. Although individual trajectories typically diverge substantially from actual air parcel paths within a week or two [Podglajen *et al.*, 2016; Bergman *et al.*, 2016], we suggest that the trajectory-based calculations at least provide a qualitative picture of longitudinal and height variations in convective influence. Moreover, we are not relying on the accuracy of source location information from individual 40 day trajectories; rather, we are calculating statistics of time since most recent convective influence using ensembles of trajectories.

The calculated frequency distributions of the number of days since most recent deep convection are plotted for the westPac and centeastPac flights in Figure 3. Curves corresponding to segments of flights in different potential temperature ranges are shown with different colors. In the next section, relative humidity distributions are shown versus temperature since this is the variable that largely controls RHI. The data indicate distinct features in temperature ranges of 185–190 K, 190–200 K, and 200–205 K. Hence, we separate the convective influence statistics into potential temperature ranges approximately corresponding to these temperature ranges. The primary contrast between the westPac and centeastPac flights is apparent in the lowermost TTL (potential temperatures below about 363 K corresponding to temperatures greater than about 200 K). Consider-

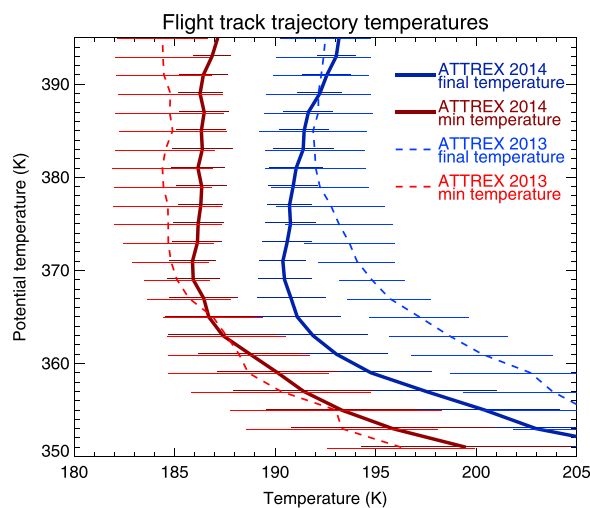


Figure 4. The mean ERA-Interim temperatures along the flight paths are plotted versus final potential temperature for the ATTREX-2014 (solid dark blue curve) and ATTREX-2013 (dashed blue curve) campaigns. Also shown are the mean minimum temperatures along 40 day back trajectories from the flight tracks (2014: solid dark red; 2013: dashed red curves). The horizontal bars indicate the standard deviations of the final and minimum temperatures.

generate frequency distributions of RHI in 1 K temperature bins (Figure 5). Times when the potential temperature was higher than 390 K are excluded to avoid excessive influence of stratospheric sampling. WestPac RHI distributions (Figures 5a–5c) are compared with those in the centeastPac (Figures 5d–5f). Several interesting features are evident. In the westPac flights, the lower TTL (temperatures greater than about 195 K) is near ice saturation ($\text{RHI} \approx 100\%$) most of the time (Figure 5a), whereas in the eastern Pacific, clear-sky lower TTL relative humidities are typically very low (Figures 5d and 5e). Relative humidities are near 100% inside lower TTL clouds in the 2013 centeastPac measurements (Figure 5f), but as noted by *Rollins et al.* [2016], cirrus were rarely encountered in the lower to middle TTL on the centeastPac flights. The observed contrast between westPac and centeastPac lower TTL relative humidities can likely be attributed at least partly to the geographic distribution of deep convection reaching the TTL over the Pacific (see section 3). Namely, the frequent convection reaching the lower TTL in the westPac provides a steady source of ice saturated air, whereas the absence of deep convection over the centeastPac implies that the lower TTL airmasses have been subsiding and drying (at levels where radiative cooling prevails) for weeks since their most recent encounters with humid air detrained from deep convection.

At the lowest temperatures sampled (185–190 K), RHI values near 100% occur most of the time, even in clear-sky regions. If we follow an air parcel upward through the TTL, it will necessarily be saturated (or supersaturated) with respect to ice when it reaches its coldest temperature along its trajectory. Therefore, it makes sense that air sampled at the lowest TTL temperatures will typically be near ice saturation. Subsaturated air is sometimes encountered even at temperatures as low as 185 K. These cases presumably correspond to air parcels that have previously experienced even lower temperatures.

At temperatures between about 190 and 200 K, low relative humidities occur frequently outside of clouds (Figures 5b and 5e), and the highest-probability RHI values approximately follow a constant H_2O mixing ratio curve (dotted curve in Figure 5 corresponding to a parcel undergoing adiabatic ascent/descent with a mixing ratio of about 2 ppmv at 100 hPa). In the centeastPac data, the predominance of dry air extends to temperatures above 200 K (Figure 5e). We hypothesize that prevalence of air dehydrated to such low mixing ratios through much of the TTL stems from the combination of slow vertical advection (implying long residence times) and large temperature variations driven by both waves and horizontal advection through regional

the 2013 flight tracks in the lower TTL (on average up to 7 K warmer at around 365 K altitude). Air parcels sampled in the lower TTL during 2013 and 2014 experienced similar minimum temperatures (primarily because most of the trajectories from the centeastPac flight tracks passed through the western Pacific cold pool).

The tropical tropopause temperatures are sensitive to the phase of the Quasi-Biennial Oscillation (QBO) [*Baldwin et al.*, 2001]. The QBO was in the easterly phase during the 2013 ATTREX deployment and the westerly phase during the 2014 deployment. Correspondingly, the tropopause temperatures were 1–2 K colder in 2013. Both the 2013 and 2014 deployments occurred in near-neutral ENSO periods.

4. TTL Relative Humidity Distributions Over the Pacific

We use the ATTREX DLH water vapor and MMS meteorological measurements to

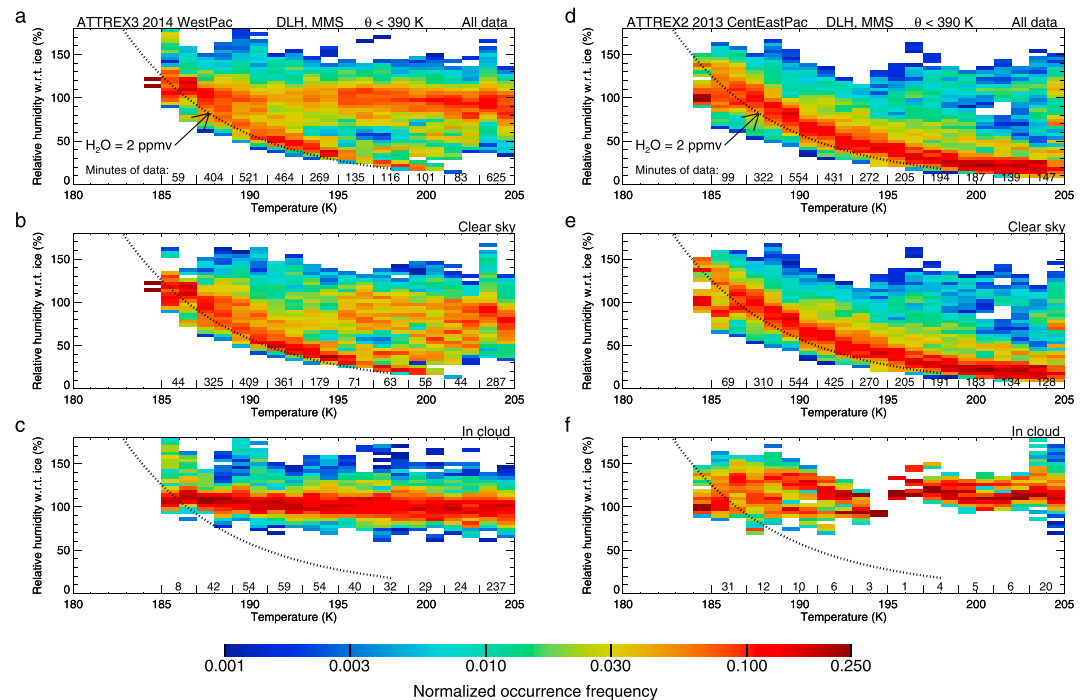


Figure 5. Frequency distributions of relative humidity with respect to ice are plotted in 1 K temperature ranges. (a–c) Data from the 2014 western Pacific campaign; (d–f) data from the 2013 eastern and central Pacific campaign. Figures 5a and 5d include all data, Figures 5b and 5e include only clear-sky data, and Figures 5c and 5f include only measurements made inside cirrus. Clear-sky measurements correspond to samples with no ice detected by FCDP and 2D-S, and in-cloud measurements correspond to ice concentrations greater than 15 L^{-1} . In order to avoid excessive influence of stratospheric samples on the statistics, we only include measurements made below 390 K potential temperature. The distributions are normalized by dividing by the total number of measurements within each temperature bin, and the color scale is logarithmic. Relative humidities were calculated using DLH water vapor, MMS temperature, and MMS pressure measurements. The black dotted curve corresponds to a parcel with a constant H_2O mixing ratio of 2 ppmv at 100 hPa undergoing adiabatic ascent/descent through the TTL. Numbers at the bottom of each figure indicate the minutes of sampling within 2 K temperature ranges. Note the limited in-cloud sampling in the central/eastern Pacific middle TTL.

temperature variations [Holton and Gettelman, 2001]. These factors imply that most air in the middle to upper TTL has experienced low temperatures and has been dehydrated to correspondingly low H_2O mixing ratios.

The temperature statistics shown in Figure 4 also help to explain the nearly constant water vapor mixing ratio observed in the middle and upper TTL (Figure 5). For potential temperatures above about 368 K, most air parcels experienced relatively cold ($\approx 187 \text{ K}$ or colder) temperatures within the previous 40 days. Thus, most of the air parcels had been dehydrated to H_2O mixing ratios of about 2 ppmv. Some of these dessicated parcels have subsequently warmed considerably, resulting in very low relative humidities.

Across the entire temperature range, observed relative humidities were near ice saturation when ice concentrations exceeded 15 L^{-1} (the in-cloud data shown in Figures 5c and 5f). In the centeastPac, the in-cloud RHI distributions at temperatures above about 188 K are noisy because few clouds were sampled. Even in the westPac, there is some scatter around $\text{RHI} = 100\%$ inside TTL cirrus, which can be attributed to both measurement uncertainty (about 10–15%) and real supersaturation and subsaturation in the clouds [Rollins et al., 2016]. The time scales for quenching of supersaturation in TTL cirrus (which typically have relatively low ice concentrations) can be on the order of hours [Jensen et al., 2013], and wave-driven temperature oscillations can force relative humidities well away from 100% within the clouds [Krämer et al., 2009].

We note here that all of the features described above are also apparent when we generate the RHI distributions using the NOAA- H_2O measurements instead of DLH measurements (not shown). The agreement between the two independent water vapor data sets provides increased assurance that the RHI distributions are not a result of measurement biases.

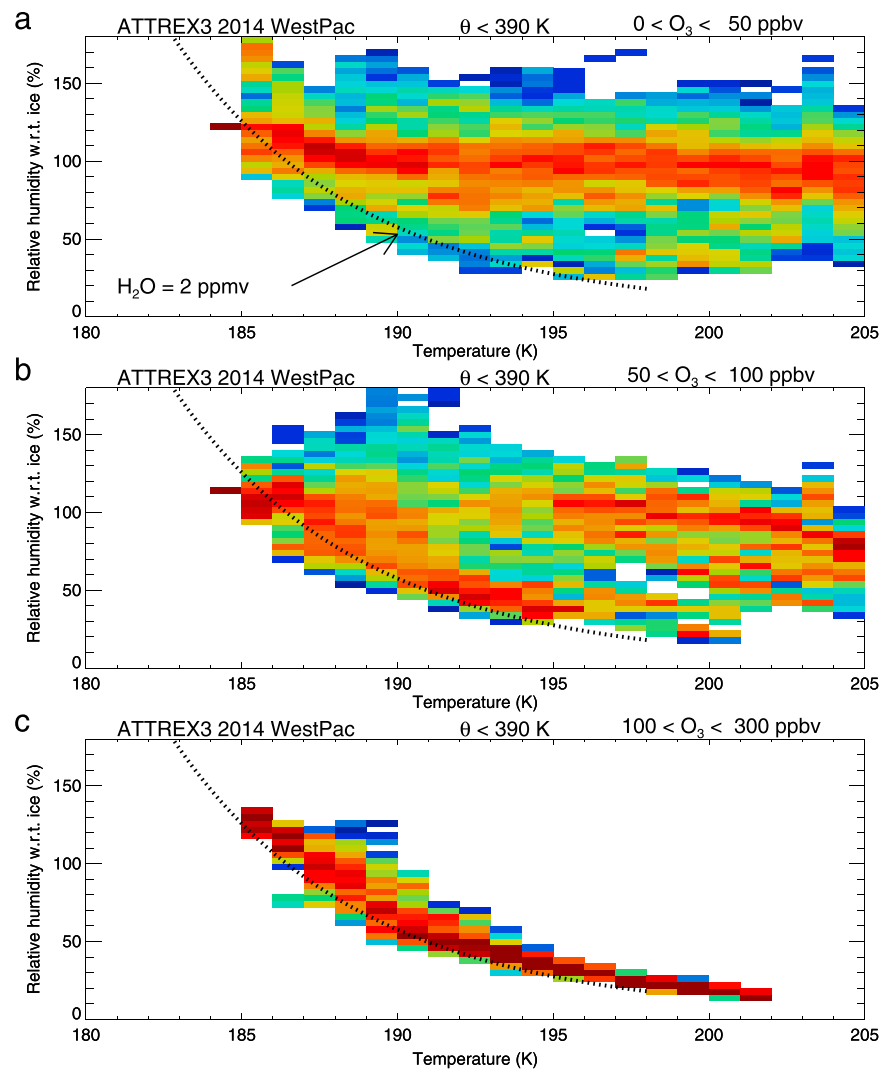


Figure 6. Same as Figure 5 except that the data have been subsetted into ranges of measured ozone concentration. (a) $O_3 < 50$ ppbv; (b) $50 < O_3 < 100$ ppbv; and (c) $100 < O_3 < 300$ ppbv. Both clear-sky and in-cloud data are included.

Further insight can be gained from subdividing the western Pacific data into different ranges of measured ozone concentration (Figure 6). As noted by *Rex et al.* [2014] and *Pan et al.* [2015], relatively low ozone concentrations (<50 ppbv) commonly occur in the upper troposphere over the western Pacific, primarily resulting from frequent deep convective transport of clean maritime air to the upper troposphere [*Folkins et al.*, 2002; *Pan et al.*, 2013]. In air masses sampled near or above the tropopause, higher ozone concentrations generally occur, primarily as a result of mixing with ozone-rich stratospheric air, but photochemical production of ozone and transport from polluted regions can also play important roles [*Ploeger et al.*, 2011]. In the western Pacific air masses sampled with $O_3 < 50$ ppbv, RHI values near 100% prevail across the entire temperature range. The high frequency of saturated air in the low ozone regions sampled is consistent with low ozone indicating relatively recent detrainment from maritime deep convection. Since deep convection detrains large amounts of ice, air masses recently detrained from deep convection will necessarily have relative humidities near 100%. When the ozone concentration is somewhat higher (50–100 ppbv, Figure 6b), lower relative humidities begin to dominate the statistics in the middle TTL (at temperatures between about 190 and 195 K). In air sampled with even higher ozone concentrations corresponding to the lower stratosphere (100–300 ppbv, Figure 6c), the tail of dry air extends to warmer temperatures.

In the centeastPac ATTREX measurements, ozone mixing ratios less than 50 ppbv rarely occur because of the lack of local convection reaching the TTL in the region (Figure 2). The centeastPac RHI distributions

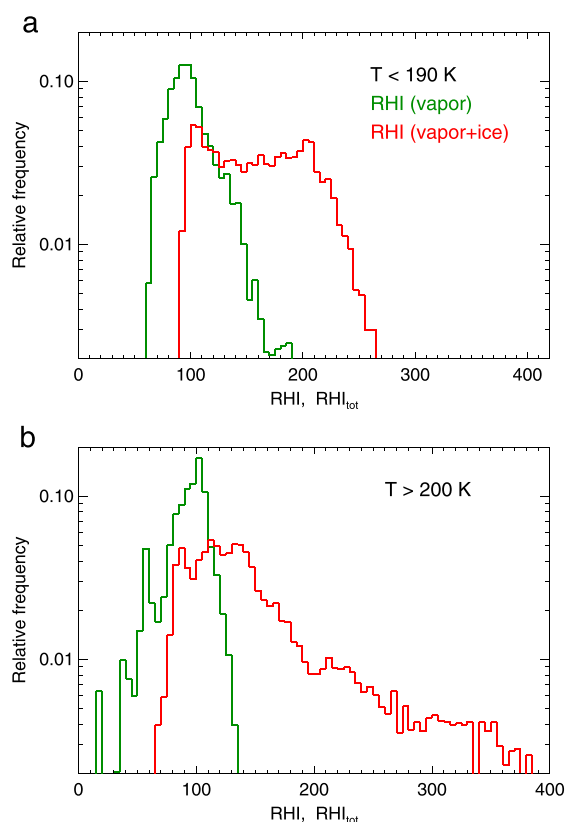


Figure 7. Frequency distributions of relative humidity with respect to ice computed with the 2014 NOAA-H₂O vapor measurements (green curves) and total water measurements (red curves). (a) Temperatures less than 190 K (upper TTL); (b) temperatures greater than 200 K (lower TTL).

temperatures (Figure 4). As shown in Figure 8, the lower TTL water vapor mixing ratios are also quite different in the westPac and centeastPac. Most of the lower TTL measurements in the centeastPac indicated H₂O mixing ratios of a few parts per million (similar to the upper TTL and suggesting subsidence of dry air from the tropopause region into the lower TTL), whereas values ranging from 10–20 ppmv predominate in the western Pacific lower TTL measurements.

5. Simulations of TTL Relative Humidity

For simulation of RHI distributions in the air masses sampled during ATTREX, we use the semi-Lagrangian, one-dimensional cloud model described by *Jensen and Pfister* [2004] and *Ueyama et al.* [2014, 2015]. Specifically, following *Ueyama et al.* [2014], we run 40 day diabatic back trajectories from times and locations along each of the ATTREX 2013 and 2014 flight tracks in the tropics using ERA-Interim horizontal winds and diabatic heating rates calculated off-line by *Yang et al.* [2010]. The trajectory curtain spacing along the flight tracks is the same as for the parcel trajectories described above (every 0.3° horizontal distance or 0.2 km vertical distance, whichever is smaller). Along each of these trajectories, we extract vertical profiles of temperature from the ERA-Interim fields. The resulting temperature curtains (temperature versus height and time along the trajectories) are used to drive one-dimensional simulations of TTL cirrus formation and water vapor. The model tracks thousands of individual ice crystals to represent the clouds, and physical processes simulated include homogeneous freezing ice nucleation, sedimentation, deposition growth, and sublimation.

As described by *Ueyama et al.* [2014, 2015], the influence of deep convection on the vertical profile of humidity in the model is treated by tracing the trajectories through geostationary satellite infrared fields of convective cloud top height. Whenever the trajectories pass through convective clouds with heights extending into the TTL, we set the humidity profile up to the cloud top to the saturation mixing ratio.

for ozone mixing ratio ranges of 50–100 ppbv and 100–300 ppbv look similar to each other except that the water vapor mixing ratios in the lower ozone subset are somewhat higher than those in the higher-ozone subset at temperatures greater than 190 K (not shown).

The contrast between the western Pacific lower and upper TTL can be further examined by comparing the frequency distributions of total water (vapor plus ice). We use the 2014 NOAA forward facing inlet measurements of vapor and condensed mass to compute these distributions at temperatures less than 190 K (upper TTL) and greater than 200 K (lower TTL), with the temperature limits guided by the RHI distributions shown in Figure 5. In order to facilitate direct comparison of the different temperature regimes, we compute relative humidities by dividing the total water vapor mixing ratios by the saturation mixing ratio. As shown in Figure 7, the RHI calculated from western Pacific total water measurements shows more variability in the lower TTL than in the upper TTL, presumably because of the intermittent injections of ice and vapor by deep convection.

Several factors likely contribute to the stark contrast between the westPac and centeastPac lower TTL clear-sky relative humidities (Figure 5), including the contrast in convective influence (Figures 2 and 3) and the contrast in

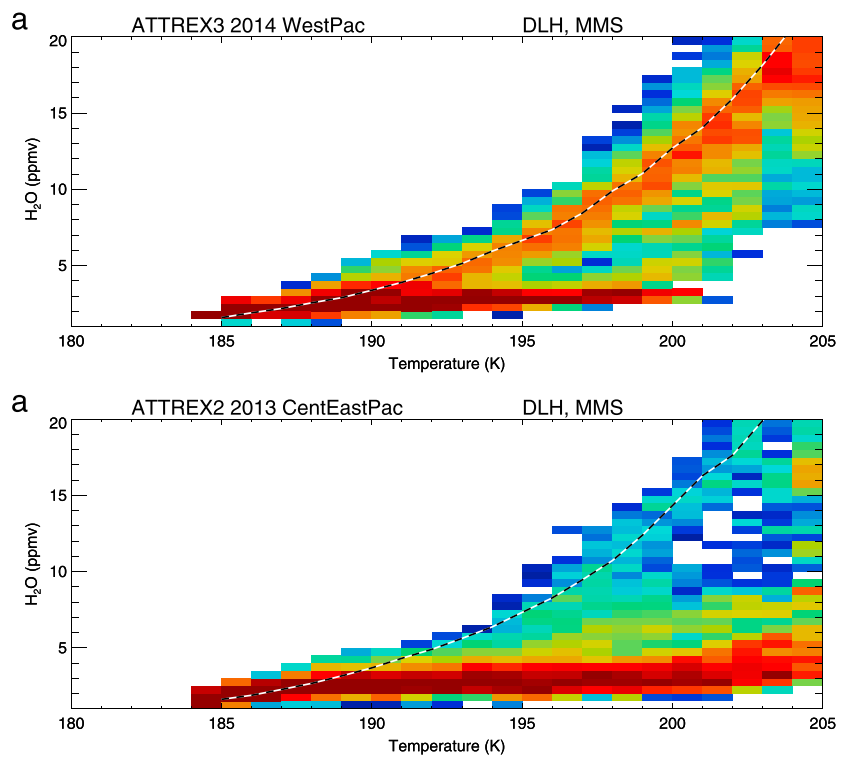


Figure 8. Same as Figure 5 except that water vapor mixing ratio frequency distributions are shown for the (top) 2014 and (bottom) 2013 campaigns. The dashed line shows the saturation mixing ratio versus temperature.

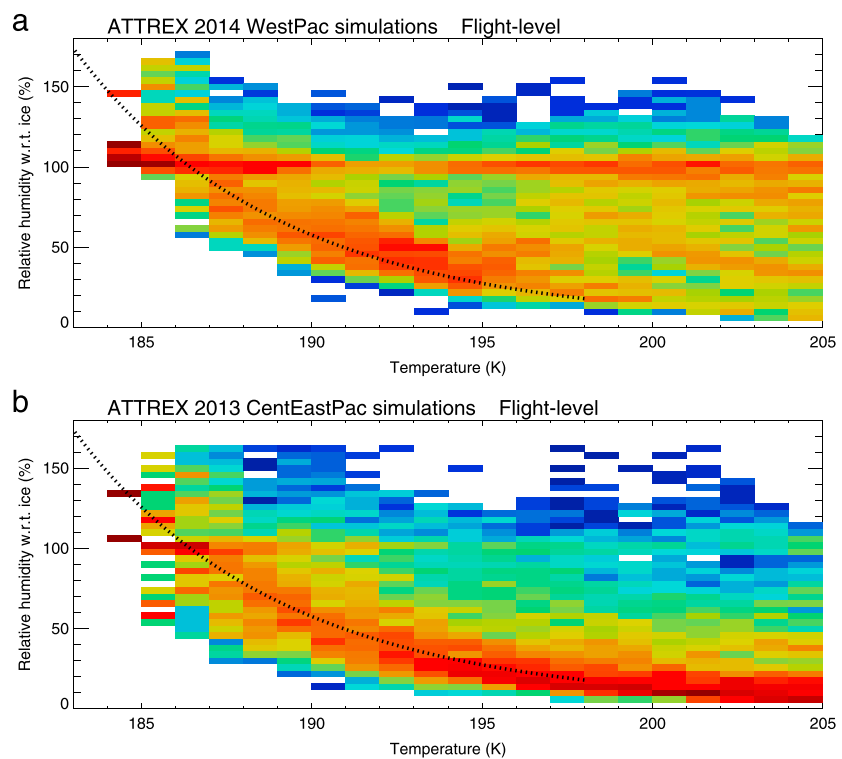


Figure 9. Simulated frequency distributions of relative humidity versus temperature along the ATTREX-2014 (western Pacific) and ATTREX-2013 (central and eastern Pacific) flight tracks. The dotted lines indicating 2 ppmv H₂O mixing ratio are included to facilitate comparison with the measured RHI frequency distributions (Figure 5).

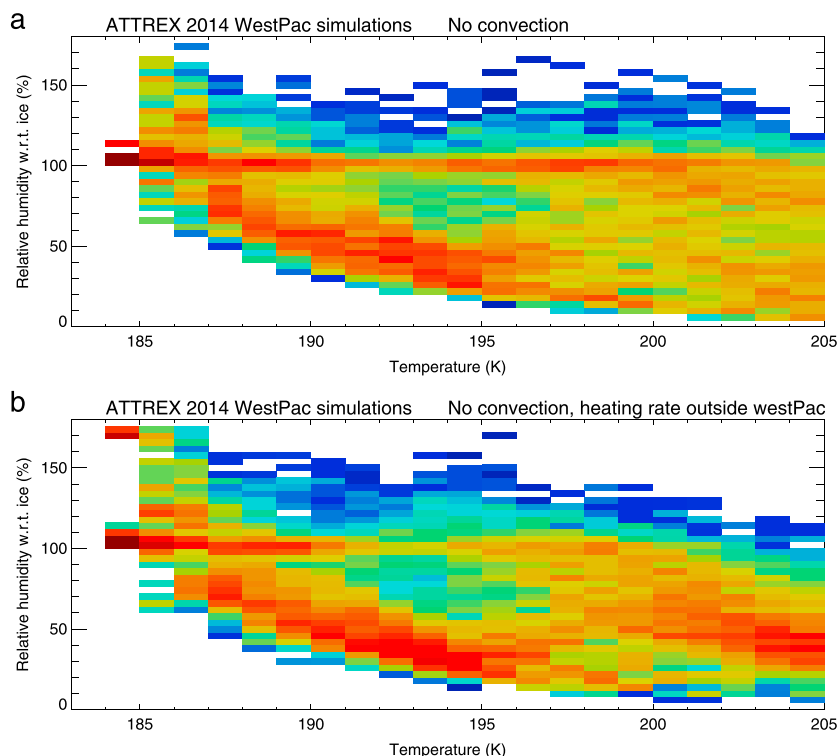


Figure 10. Sensitivity tests showing the impact on simulated ATTREX-2014 (WestPac) RHI frequency distribution of (top) excluding convective influence and (bottom) excluding convection as well as using the heating rate profile from the tropics outside the western Pacific.

Ice detrained from deep convection can enhance TTL humidity if the ice crystals sublimate before precipitating out. However, we find that the contrast in east-west RHI distributions noted here is not significantly altered by inclusion of detrained ice. We have chosen to avoid including this process in the simulations presented here because of the large uncertainty in assumed mass and size of the detrained ice crystals.

The water vapor profiles in these simulations are initialized with MLS observations; however sensitivity experiments indicate that changing the initial humidity profiles has no significant impact on the final humidity profiles.

For comparison with the aircraft measurements of RHI frequency distributions, we compute the distributions of RHI at the final times in the trajectory curtain simulations and at the potential temperatures corresponding to the aircraft altitudes along the flight tracks. The distributions of relative humidity versus temperature from simulations along the ATTREX-2014 and ATTREX-2013 flights with convective influence included are shown in Figure 9. The trajectory curtain simulations reproduce most of the features seen in the observed RHI frequency distributions (Figures 5a and 5d). The simulated western Pacific RHI frequency distribution shows predominance of saturated air in the upper and lower TTL. The simulated centeastPac RHI frequency distribution shows that high relative humidities are common at the lowest temperature, but dry air dominates in the lower TTL (in agreement with the measurements). The middle to upper TTL (temperature less than about 195 K) RHs in the model are somewhat lower than indicated by the observations. We hypothesize that this difference is related to the somewhat higher ice concentrations produced in the model by homogeneous freezing than indicated by the ATTREX TTL cirrus measurements [see *Jensen et al.*, 2016a]. The numerous ice crystals in the simulations deplete vapor in excess of saturation more effectively than what occurs in the real atmosphere.

As a test of the hypothesis that the saturated air in the western-Pacific lower TTL is driven by convective influence, we ran the simulations with convective influence excluded from the model. The resulting RHI frequency distributions (Figure 10a) do indicate more frequent occurrence of dry air at the warmest temperatures than in the simulations with convective influence, but saturation still prevails much of the time. As discussed above,

the vertical level of zero radiative heating is particularly low over the western Pacific, implying that air is essentially rising throughout the TTL over this region, which will raise the relative humidity. To investigate whether the eastern/western Pacific contrast in lower TTL relative humidities could be partly attributed to the geographic distribution of TTL vertical motion, we ran the ATTREX-2014 simulations both excluding convective influence and using the tropical-mean heating rate profile including only regions outside the western Pacific. The resulting RHI frequency distribution (Figure 10b) shows that the relative humidities were further reduced near the very bottom of the TTL where subsidence prevails outside the westPac TTL. However, the simulated that lower TTL westPac relative humidities are still higher than the observed centeastPac values. These results suggest that the east/west contrast in lower TTL relative humidity over the Pacific is not entirely attributable to differences in convective influence and vertical motion. The temperature contrast also seems to be an important factor. Note that the westPac simulation including convection (Figure 9a) best reproduces the observed absence of dry air in the lower TTL.

6. Summary and Discussion

We have used airborne in situ measurements of water vapor, temperature, pressure, and ozone to quantify the distribution of relative humidity with respect to ice over the Pacific versus temperature and longitude during the late January through early March time period. A number of notable features are evident in the measured RHI distributions (see Figure 5):

1. The lower TTL (temperatures greater than about 195 K) relative humidity is typically near ice saturation in the western Pacific, but very low relative humidities were measured most of the time in the central/eastern Pacific.
2. As expected, relative humidities near ice saturation ($\text{RHI} = 100\%$) occur most of the time when the aircraft was sampling inside TTL cirrus, although substantial in-cloud supersaturations and subsaturations exist. As discussed by [Krämer *et al.*, 2009], observed supersaturation/subsaturation within cirrus can be maintained by wave-driven updrafts/downdrafts.
3. At the lowest temperatures sampled (<190 K), the relative humidity is typically near or above 100%, presumably because even lower temperatures and dehydration to lower H_2O concentrations did not routinely occur upstream of the coldest air parcels sampled. In other words, at the locations where very cold air was encountered by the aircraft, the air parcels sampled were often near their minimum temperatures.
4. At temperatures between about 190 and 200 K, low relative humidities and approximately constant water vapor mixing ratios of ≈ 2 ppmv occur frequently, indicating that most of the air masses in the middle to upper TTL over the Pacific had experienced cold temperatures and dehydration to low H_2O mixing ratios.
5. In air masses sampled with relatively low ozone concentration (<50 ppbv), relative humidities are near 100% across the entire TTL temperature range over the western Pacific, consistent with the expectations that the low ozone in the TTL is driven by deep convective transport from the clean, maritime lower troposphere, and air detrained from deep convection will be saturated with respect to ice.

The general features of the RHI distributions are consistent with the late winter meteorological environment over the Pacific. Convective transport to the lower TTL occurs much more frequently over the western Pacific than over the central/eastern Pacific (Figure 2), which no doubt contributes to the contrast between the high relative humidities observed in the western Pacific flights and the much lower humidities measured in the central/eastern Pacific lower TTL. Trajectory analysis shows that lower TTL air parcels sampled in the central/eastern Pacific had experienced similar minimum temperatures as those sampled in the western Pacific, even though the central/eastern lower TTL air masses sampled were much warmer than those in the western Pacific (Figure 4). This contrast contributes to the observed east-west gradient in relative humidities, although the water vapor mixing ratios were also much lower in the central/eastern Pacific lower TTL measurements (Figure 8). Long-range transport also plays an important role, since the low H_2O mixing ratios sampled in the central/eastern Pacific were typically set when the air parcels passed through the coldest temperatures in the western Pacific.

We have also used one-dimensional simulations along trajectories driven by meteorological analysis fields to simulate the relative humidities along the aircraft flight tracks. The cloud model used includes the important effects of ice nucleation, ice crystal deposition growth, and sedimentation on TTL water vapor concentration. Convective influence on TTL humidity is included using satellite measurements of convective cloud top height, and temperature oscillations driven by waves not resolved by the analyses are included.

The simulations generally reproduce the RHI distribution features indicated by the observations (Figure 9). Sensitivity tests indicate that although the geographic distributions of convective influence and TTL vertical motion contribute to the east-west contrast in lower TTL relative humidity, these factors alone do not entirely explain the observed contrast, and the warmer centeastPac temperatures are likely a strong contributing factor. Nonetheless, the simulations show the strong sensitivity of TTL relative humidities to convective influence and vertical motion. Comparison between global-model distributions of RHI and observed distributions should be useful for evaluation of the representations of convective influence and vertical motion in the models.

Acknowledgments

This work was supported by NASA's Airborne Tropical Tropopause Experiment project. The data used in this study are openly available on the NASA Earth Science Project Office website (espoarchive.nasa.gov).

References

- Baldwin, M. P., et al. (2001), The quasi-biennial oscillation, *Rev. Geophys.*, *39*, 179–229.
- Bergman, J. W., E. J. Jensen, L. Pfister, and Q. Wang (2012), Seasonal differences of vertical-transport efficiency in the tropical tropopause layer: On the interplay between tropical deep convection, large-scale vertical ascent, and horizontal circulations, *J. Geophys. Res.*, *117*, D05302, doi:10.1029/2011JD016992.
- Bergman, J. W., E. J. Jensen, L. Pfister, and T. V. Bui (2016), Air parcel trajectory dispersion near the tropical tropopause, *J. Geophys. Res. Atmos.*, *121*, 3759–3775, doi:10.1002/2015JD024320.
- Fahey, D. W., et al. (2014), The AquaVIT-1 intercomparison of atmospheric water vapor measurement techniques, *Atmos. Meas. Tech.*, *7*, 3177–3213.
- Folkens, I., C. Braun, A. M. Thompson, and J. White (2002), Tropical ozone as indicator of deep convection, *J. Geophys. Res.*, *107*, 4184, doi:10.1029/2001JD001178.
- Forster, P. M. F., and K. P. Shine (2002), Assessing the climate impact of trends in stratospheric water vapor, *Geophys. Res. Lett.*, *29*, 1086, doi:10.1029/2001GL013909.
- Gao, R.-S., J. Ballard, L. A. Watts, T. D. Thornberry, S. J. Cliviora, R. J. McLaughlin, and D. W. Fahey (2012), A compact, fast UV photometer for measurement of ozone from research aircraft, *Atmos. Meas. Tech.*, *5*, 2201–2210.
- Gettelman, A., P. M. de F. Forster, M. Fujiwara, Q. Fu, H. Vömel, L. K. Gohar, C. Johanson, and M. Ammerman (2004), Radiation balance of the tropical tropopause layer, *J. Geophys. Res.*, *109*, D07103, doi:10.1029/2003JD004190.
- Holton, J., and A. Gettelman (2001), Horizontal transport and dehydration of the stratosphere, *Geophys. Res. Lett.*, *28*, 2799–2802.
- Jensen, E. J., and L. Pfister (2004), Transport and freeze-drying in the tropical tropopause layer, *J. Geophys. Res.*, *109*, D02207, doi:10.1029/2003JD004022.
- Jensen, E. J., et al. (2008), Formation of large ($\approx 100 \mu\text{m}$) ice crystals near the tropical tropopause, *Atmos. Chem. Phys.*, *8*, 1621–1633.
- Jensen, E. J., G. Diskin, R. P. Lawson, S. Lance, T. P. Bui, D. Hlavka, M. McGill, L. Pfister, O. B. Toon, and R.-S. Gao (2013), Ice nucleation and dehydration in the Tropical Tropopause Layer, *Proc. Natl. Acad. Sci. U.S.A.*, *110*(6), 2041–2046, doi:10.1073/pnas.1217104110.
- Jensen, E. J., et al. (2016a), On the susceptibility of cold tropical cirrus to ice nuclei abundance, *J. Atmos. Sci.*, *73*, 2445–2464, doi:10.1175/JAS-D-15-0274.1.
- Jensen, E. J., et al. (2016b), The NASA Airborne Tropical Tropopause Experiment (ATTREX): High-altitude aircraft measurements in the tropical western Pacific, *Bull. Am. Meteorol. Soc.*, *98*(1), 129–143, doi:10.1175/BAMS-D-14-00263.1.
- Kelly, K. K., M. H. Proffitt, K. R. Chan, M. Loewenstein, J. R. Podolske, S. E. Strahan, J. C. Wilson, and D. Kley (1993), Water vapor and cloud water measurements over Darwin during the step 1987 tropical mission, *J. Geophys. Res.*, *98*, 8713–8723.
- Kim, J.-E., M. J. Alexander, T. P. Bui, J. M. Dean-Day, R. P. Lawson, S. Woods, D. Hlavka, L. Pfister, and E. J. Jensen (2016), Ubiquitous influence of waves on tropical high cirrus cloud, *Geophys. Res. Lett.*, *43*, 5895–5901, doi:10.1002/2016GL069293.
- Kley, D., A. L. Schmeltekopf, K. Kelly, R. H. Winkler, T. L. Thompson, and M. McFarland (1982), Transport of water through the tropical tropopause, *Geophys. Res. Lett.*, *9*, 617–620.
- Kley, D., H. G. Smit, H. Vömel, H. Grassl, V. Ramanathan, P. J. Crutzen, S. Williams, J. Meywerk, and S. J. Oltmans (1997), Tropospheric water vapour and ozone cross-sections in a zonal plane over the central equatorial Pacific Ocean, *Q. J. R. Meteorol. Soc.*, *123*, 2009–2040.
- Krämer, M., C. Schiller, A. Afchine, I. Gensch, A. Mangold, N. Spelten, N. Sitnikov, S. Boormann, M. de Reus, and P. Spichtinger (2009), Ice supersaturations and cirrus cloud crystal numbers, *Atmos. Chem. Phys.*, *9*, 3505–3522.
- Lance, S., C. A. Brock, D. Rogers, and J. A. Gordon (2010), Water droplet calibration of the Cloud Droplet Probe (CDP) and in-flight performance in liquid, ice and mixed-phase clouds during ARCPAC, *Atmos. Meas. Tech.*, *3*, 1683–1706.
- Lawson, R. P., B. A. Baker, B. Pilson, and Q. Mo (2006), In situ observations of the microphysical properties of wave, cirrus and anvil clouds. Part II: Cirrus clouds, *J. Atmos. Sci.*, *63*, 3186–3203.
- O'Connor, D., B. Baker, and R. P. Lawson (2008), Upgrades to the FSSP-100 electronics. International Conference on Clouds and Precipitation, Cancun, Mexico. [Available at http://convention-center.net/iccp2008/abstracts/Program_on_line/Poster_13/OConnor_extended_final.pdf, 7–11 July.]
- Pan, L. L., L. C. Paulik, S. B. Honomichi, L. A. Munchak, J. Bian, H. B. Selkirk, and H. Vömel (2013), Identification of the tropical tropopause transition layer using the ozone-water vapor relationship, *J. Geophys. Res. Atmos.*, *119*, 3586–3599, doi:10.1002/2013JD020558.
- Pan, L. L., et al. (2015), Bimodal distribution of free tropospheric ozone over the tropical western Pacific revealed by airborne observations, *Geophys. Res. Lett.*, *42*, 7844–7851, doi:10.1002/2015GL065562.
- Pfister, L., H. B. Selkirk, E. J. Jensen, M. R. Schoeberl, O. B. Toon, E. V. Browell, W. B. Grant, B. Gary, M. J. Mahoney, T. V. Bui, and E. Hints (2001), Aircraft observations of thin cirrus clouds near the tropical tropopause, *J. Geophys. Res.*, *106*, 9765–9786.
- Ploeger, F., S. Fueglistaler, J. U. Gross, G. Günther, P. Konopka, Y. S. Liu, R. Müller, F. Ravengnani, C. Schiller, A. Ulanovski, and M. Riese (2011), Insight from ozone and water vapour on transport in the Tropical Tropopause Layer (TTL), *Atmos. Chem. Phys.*, *11*, 407–419.
- Podglajen, A., A. Hertzog, R. Plougonven, and N. Žagar (2016), Assessment of the accuracy of (re)analyses in the equatorial lower stratosphere, *J. Geophys. Res. Atmos.*, *119*, 11,166–11,188, doi:10.1002/2014JD021849.
- Podolske, J. R., G. W. Sachse, and G. S. Diskin (2003), Calibration and data retrieval algorithms for the NASA Langley/Ames Diode Laser Hygrometer for the NASA Transport and Chemical Evolution Over the Pacific (TRACE-P) mission, *J. Geophys. Res.*, *108*, 8792, doi:10.1029/2002JD003156.
- Rex, M., et al. (2014), A tropical West Pacific OH minimum and implications for stratospheric composition, *Atmos. Chem. Phys.*, *14*, 4827–4841.
- Riese, M., F. Ploeger, A. Rap, B. Vogel, P. Konopka, M. Dameris, and P. Forster (2012), Impact of uncertainties in atmospheric mixing on simulated UTLS composition and related radiative effects, *J. Geophys. Res.*, *117*, D16305, doi:10.1029/2012JD017751.

- Rollins, A. W., T. D. Thornberry, R. S. Gao, S. Woods, R. P. Lawson, T. P. Bui, E. J. Jensen, and D. W. Fahey (2016), Observational constraints on the efficiency of dehydration mechanisms in the tropical tropopause layer, *Geophys. Res. Lett.*, *43*, 2912–2918, doi:10.1002/2016GL067972.
- Schiller, C., J.-U. Gross, P. Konopka, F. Plöger, F. H. S. dos Santos, and N. Spelton (2009), Hydration and dehydration at the tropical tropopause, *Atmos. Chem. Phys.*, *9*, 9647–9660.
- Scott, S. G., T. P. Bui, K. R. Chan, and S. W. Bowen (1990), The meteorological measurement system on the NASA ER-2 aircraft, *J. Atmos. Oceanic Technol.*, *7*, 525–540.
- Solomon, S., K. Rosenlof, R. Portmann, J. Daniel, S. Davis, T. Sanford, and G.-K. Plattner (2010), Contributions of stratospheric water vapor changes to decadal variations in the rate of global warming, *Science*, *327*, 1219–1223.
- Thornberry, T. D., A. W. Rollins, R. S. Gao, L. A. Watts, S. J. Ciciora, R. J. McLaughlin, and D. W. Fahey (2015), A two-channel, tunable diode laser-based hygrometer for measurement of water vapor and cirrus cloud ice water content in the upper troposphere and lower stratosphere, *Atmos. Meas. Tech.*, *8*, 211–244.
- Ueyama, R., L. Pfister, E. J. Jensen, G. S. Diskin, T. P. Bui, and J. M. Dean-Day (2014), Dehydration in the tropical tropopause layer: A case study for model evaluation using aircraft observations, *J. Geophys. Res. Atmos.*, *119*, 5299–5316, doi:10.1002/2013JD021381.
- Ueyama, R., E. J. Jensen, L. Pfister, and J.-E. Kim (2015), Dynamical, convective, and microphysical control on wintertime distributions of water vapor and clouds in the tropical tropopause layer, *J. Geophys. Res. Atmos.*, *120*, 10,483–10,500, doi:10.1002/2015JD023318.
- Vömel, H., et al. (2002), Balloon-borne observations of water vapor and ozone in the tropical upper troposphere and lower stratosphere, *J. Geophys. Res.*, *107*, 4210, doi:10.1029/2001JD000707.
- Weinstock, E. M., E. J. Hints, A. E. Dessler, J. F. Oliver, N. L. Hazen, J. N. Demusz, N. T. Allen, L. B. Lapson, and J. G. Anderson (1994), New fast response photofragment fluorescence hygrometer for use on the NASA ER-2 and the Perseus remotely piloted aircraft, *Rev. Sci. Instrum.*, *22*, 3544–3554.
- Yang, Q., Q. Fu, and Y. Hu (2010), Radiative impacts of clouds in the tropical tropopause layer, *J. Geophys. Res.*, *115*, D00H12, doi:10.1029/2009JD012393.